IEEE Access
Multidisciplinary ⋮ Rapid Review ⋮ Open Access Journal

Received 21 July 2026, accepted 28 August 2026, date of publication 2 September 2026, date of current version 15 September 2026.

Digital Object Identifier 10.1109/ACCESS.2026.3730198

RESEARCH ARTICLE

Façade Cleaning Robot for Convex-Shaped Infrastructure: Design and Experiment

SAHOON AHN[1], YECHEOL MOON[2], JOONHYUK KWON[1], JIHONG KIM[1], HYUNGCHAN JOO[1], DOYOUNG PARK[1], HWA SOO KIM[3], (Senior Member, IEEE), AND TAEWON SEO[1], (Senior Member, IEEE)

[1]School of Mechanical Engineering, Hanyang University, Seoul 04763, South Korea
[2]Advanced Robotics Research Center, Korea Institute of Machinery and Materials (KIMM), Daejeon 34103, South Korea
[3]Department of Mechanical System Design, Kyonggi University, Suwon 16227, South Korea

Corresponding author: TaeWon Seo (taewonseo@hanyang.ac.kr)

This work was supported in part by the National Research Foundation of Korea (NRF) grant funded by the Ministry of Science and ICT for the Bridge Convergence Research and Development Program under Grant NRF-2021M3C1C3096807 and Grant NRF-2021M3C1C3096808; in part by the Institute of Information and Communications Technology Planning and Evaluation (IITP) grant funded by Korean Government (MSIT) under Grant RS-2025-02304968; in part by the ANCHOR through Seoul ANCHOR Center, funded by the Ministry of Education (MOE); in part by Seoul Metropolitan Government under Grant 2026-ANCHOR-01-027-04; in part by the National Research Foundation of Korea (NRF) grant funded by Korea Government (MSIT) under Grant RS-2026-25475421; in part by the Ministry of Trade, Industry and Energy (MOTIE); and in part by Korea Evaluation Institute of Industrial Technology (KEIT) under Grant RS-2024-00443400.

ABSTRACT This study developed an integrated robot platform, Edelstro-S, for managing complex-shaped building exteriors, addressing two key limitations of existing ascender robots: insufficient wall adaptation capability and workspace constraints. The hybrid system integrates ascender, wheel-leg, and anchor subsystems, in which the ascender defines a rope-length-constrained workspace and the wheel-leg subsystem provides high-speed surface movement and obstacle traversal within it. Mathematical modeling was used to analyze the workspace and singularity characteristics of the cable-driven parallel ascender mechanism, as well as the kinematics and static stability of the wheel-leg subsystem. Component-level and system-integration tests were conducted on the fabricated 79.75 kg platform in both laboratory and outdoor environments. The results show an ascending speed of 21.84 m/min and a descending speed of 22.93 m/min, a multisensor-fusion position estimation accuracy of 7.30 cm, successful traversal of obstacles up to 500 mm in height, stable operation under wind speeds up to 9.4 m/s, a minimum turning curvature radius of 0.4 m, and a maximum cleaning speed of 4.8 m^2/min. These results demonstrate the platform's adaptability to the irregular geometries of modern building façades and its potential to automate high-risk exterior maintenance tasks while improving worker safety.

INDEX TERMS Ascender mechanism, building maintenance, cable-driven parallel robot, façade-cleaning robot, hybrid locomotion, wheel-leg mechanism.

NOMENCLATURE

CDPR	Cable-Driven Parallel Robot.
GRF	Ground Reaction Force.
IRPM	Incompletely Restrained Positioning Mechanism.
NESM	Normalized Energy Stability Margin.
RMSE	Root Mean Square Error.
SVD	Singular Value Decomposition.

The associate editor coordinating the review of this manuscript and approving it for publication was Li He.

I. INTRODUCTION

The rapid growth of modern cities has driven a continuous increase in high-rise buildings, with the global count exceeding 1,319 as of 2017 [1], and the exterior cleaning market estimated to reach $9.67 billion by 2020 [2]. Despite ongoing safety regulations such as the United Kingdom's Defective Premises Act of 1972 [3], accidents remain prevalent: OSHA reports 88 window-cleaning incidents and 62 fatalities in the United States over the past 15 years [4], with further accidents

© 2026 The Authors. This work is licensed under a Creative Commons Attribution 4.0 License.
For more information, see https://creativecommons.org/licenses/by/4.0/

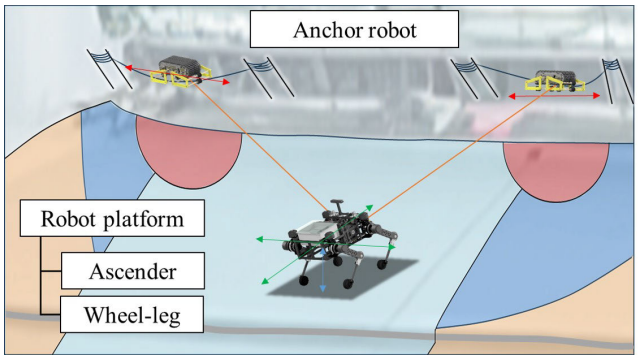

FIGURE 1. Overall structure of the integrated robot platform. The anchor robot is positioned on the upper rope to move the anchor point, and the robot platform moves along the building exterior wall using this anchor as a fixed point. The robot platform consists of an ascender and wheel-legs, and each robot can perform tasks in various environments through integrated control.

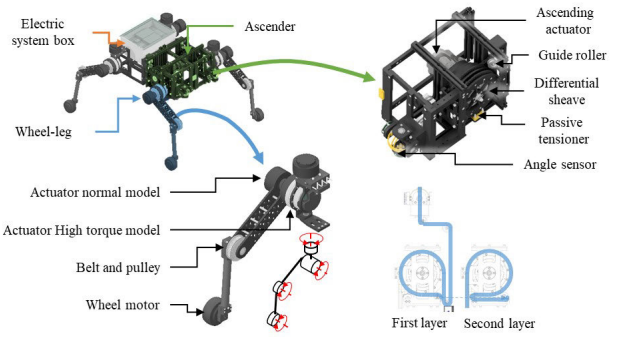

FIGURE 2. Overall hardware architecture showing the main structural components: ascender modules, four wheel-leg limbs, electronics system box, and sensors.

reported across Asia [5], [6], [7]. These figures underscore the urgent need to automate high-risk exterior maintenance tasks.

To address this, various exterior management robots have been developed, classified by locomotion type (track, wheel, walking, translation) and attachment type (vacuum suction, vortex/magnet, wire/rope, bioinspired) [8]. Representative systems include Skycleaner 3, which uses pneumatic cylinders with suction pads for translation-based movement [9], and WallWalker, which employs independently driven wheels with vacuum-based wet adhesion [10]. However, wire-based systems suffer from installation difficulty and susceptibility to surface conditions, while suction and bioinspired methods lose adhesion effectiveness on rough or uneven surfaces [11], [12].

Our research team has developed a series of rope-based wall-cleaning robots, progressively addressing challenges in ascending mechanism design [13], [14], vibration reduction [15], position control [16], obstacle traversal [17], mechanism lightweighting [18] and window recognition [19]. However, these systems share a fundamental limitation: they are designed primarily for flat, obstacle-free façades and cannot adequately respond to the irregular and complex exterior wall environments that are becoming increasingly common in modern architecture.

To overcome the workspace limitations of rope-based wall-cleaning robots, we draw upon the locomotion and obstacle-traversal capabilities of quadruped robots, which have been actively developed since 2010. These platforms are broadly classified into mammalian types, such as Spot [20] and ANYmal [21], which demonstrate robust performance on unstructured terrain, and insect types, such as TITAN-XIII [22] and ALPHRED [23], which offer flexible foot-direction control suited for complex surface interaction. Integrating such mechanisms with a rope-based ascender presents a viable path toward handling the complex façade environments that existing systems cannot address.

Conventional building exterior management relies on gondolas, aerial work platforms, and rooftop crane systems, all of which are effective only on flat vertical façades and cannot accommodate inclined walls or irregular surface geometries. While rope-based manual descent offers greater installation flexibility, it still requires fixed anchors and suffers from the same geometric constraints. Previously developed ascender robots inherit these limitations: they operate exclusively on flat, obstacle-free walls and cannot respond to structures such as piping, window frames, or balconies that interfere with the robot's movement path. Furthermore, their workspaces are strictly bounded by rope length and anchor positions, necessitating frequent manual reinstallation that significantly undermines automation efficiency. These limitations collectively demand a new platform capable of stable operation across the diverse and complex façade forms of modern buildings.

This study aims to develop an integrated robot platform, designated as Edelstro-S, for managing complex-shaped building exteriors by addressing two major limitations of existing ascender robots: insufficient wall adaptation capability and workspace constraints. The specific contributions are as follows. First, a hybrid robot platform integrating a rope-based ascender system with an insect-type wheel-leg system is developed to enable stable operation on irregular façades that existing robots cannot access. Second, the workspace and stability characteristics of each subsystem are systematically analyzed through mathematical modeling of the cable-driven parallel robot (CDPR) and wheel-leg kinematics. Third, the performance of the fabricated platform is comprehensively evaluated through both component-level and system integration tests, quantitatively measuring key indicators including vertical movement speed, position control accuracy, obstacle traversal capability, and wind resistance.

Section II introduces the design and configuration of the integrated robot platform, including hardware, electrical, and control systems. Section III presents mathematical

TABLE 1. Specifications of Integrated Façade Cleaning Robot Platform.

Specification	Value
Total weight	79.75 kg
Length	0.879 m
Width	0.926 m
Height	0.869 m
Ascending speed	21.84 m/min
Descending speed	22.93 m/min
Max working speed	4.8 m²/min
Max obstacle height	500 mm
Degree of freedom	
Legs (4 × 3 joints)	12 d.o.f.
Wheels (4 × 1 joint)	4 d.o.f.
Ascender motors	2 d.o.f.
Actuator	
Leg joints	AK 80-64 and custom
Wheels	MDH80
Ascender	ZeroError erob 90i
Sensors	
Vision	Depth camera
Positioning	encoder, GPS, IMU
Power	48 V DPU-3200
Operating system	Ubuntu 22.04 with ROS2
Operating module	Camera, cleaning
Safety features	
Emergency brake	150 ms response time
Rope tension system	Passive tensioner with spring

analyses of the ascender and wheel-leg mechanisms, covering workspace definition, kinematics, and stability. Section IV evaluates the performance of the fabricated platform through component and system integration tests. Section V summarizes the results and outlines directions for future research.

II. SYSTEM OVERVIEW

The integrated robot platform overcomes the limitations of single-robot systems by combining three cooperating subsystems: an ascender, a wheel-leg, and an anchor robot as illustrated in Figure 1. The anchor robot repositions the rope anchor point horizontally via caterpillar-driven movement, expanding the horizontal workspace; this study assumes a fixed anchor point as its vibration dynamics are under separate investigation [24]. The ascender defines the tangential workspace through rope length constraints and drives vertical and diagonal movement. The wheel-leg system provides high-speed surface movement, posture stabilization, and obstacle traversal within the ascender-defined workspace. The overall hardware configuration and arrangement of the main structural components are illustrated in Fig. 2, while the detailed specifications of the platform are summarized in Table 1.

The ascender consists of a pair of symmetric modules forming the robot's upper body. Two high-output motors drive dual differential sheaves, which wind and unwind the ropes to achieve independent length control of each rope for precise positioning. Guide rollers maintain smooth rope routing, and a passive spring-based tensioner prevents rope slack during operation. For safety, each motor includes a built-in brake with a 150 ms response time that engages by

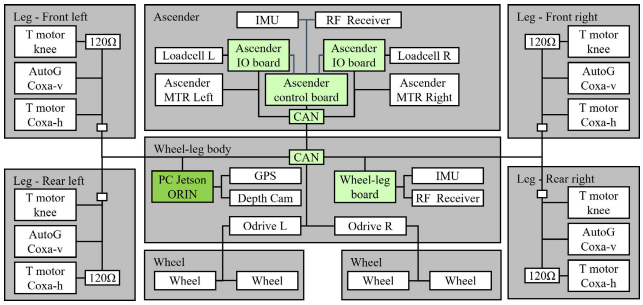

FIGURE 3. System architecture of the ascender and quadruped wheel-leg facade cleaning robot.

default upon signal loss, and a separate safety rope is attached to the body as a fall-arrest backup.

The wheel-leg system comprises four insect-type limbs, each with three rotational joints and a wheel at the tip. The insect-type configuration was selected over the mammalian type because its first joint rotates about a vertical axis, enabling direct yaw control of the foot direction. This allows diagonal and omnidirectional movement in combination with the ascender structure, which the mammalian type cannot achieve without rotating the entire body. A belt-and-pulley transmission delivers actuator torque to each independently controlled wheel, enabling both high-speed flat-surface driving and precise legged locomotion on complex terrain. Detailed kinematic analysis of both configurations is presented in Section III.

The electronics system box integrates power supply, signal processing, and control functions for the entire platform as illustrated in Fig. 3. It houses the main SBC (Jetson ORIN) for computation, a wheel-leg control board connected via CAN bus to the twelve leg joint motors, and two ODrive controllers for independent wheel actuation. A depth camera, GPS module, and IMU are incorporated for environment recognition and position estimation. The ascender subsystem operates on a dedicated control board with its own IMU and RF receiver, communicating with the wheel-leg system through integrated control.

III. ANALYSIS OF ROBOT SYSTEM

The robot platform is divided into ascender and wheel-leg subsystems, each requiring kinematic and dynamic analysis to verify operational performance. The ascender serves as the primary driving mechanism, moving the robot by winding and unwinding ropes; as an underactuated system with two motors in a 6-DOF space, it corresponds to an Incompletely Restrained Positioning Mechanism (IRPM), necessitating workspace and singularity analyses. For the wheel-leg, kinematics and stability conditions are derived to ensure safe operation on complex façades.

The analysis assumes the rope behaves as an ideal massless, inextensible cable. Physical phenomena including elastic deformation, creep, thermal elongation, sagging, and vibration have negligible influence under normal operating

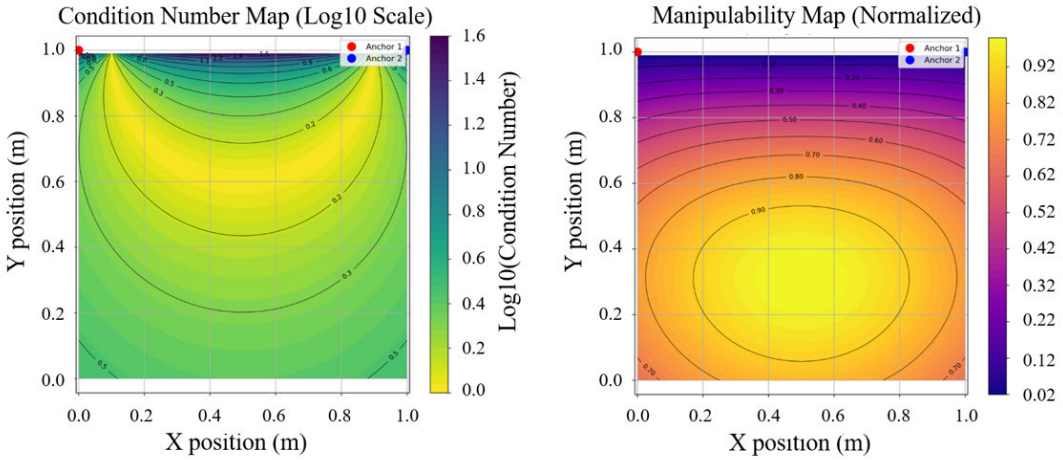

FIGURE 4. Performance maps of cable-driven parallel robot workspace. Shows condition number in log scale, normalized manipulability. Red and blue dots represent anchor positions. All maps are normalized to a 1 m × 1 m workspace, and contours represent performance gradients.

conditions through appropriate pre-tensioning and control, and modern synthetic ropes exhibit sufficiently small bending stiffness to be treated as perfectly flexible. This assumption provides sufficient accuracy for the engineering analyses that follow.

A. ASCENDER ANALYSIS

The kinematics of the ascender system are based on the geometric relationship between the robot position and rope length. The vector of the i-th rope is expressed as:

$$\mathbf{l}_i = \mathbf{p}_i - \mathbf{p}_r \tag{1}$$

where $\mathbf{p}_i$ is the position of the i-th fixed anchor [m] and $\mathbf{p}_r$ is the position of the robot's center of mass [m]. The rope lengths for inverse kinematics are obtained directly as:

$$l_1 = \|\mathbf{p}_1 - \mathbf{p}_r\| \tag{2}$$
$$l_2 = \|\mathbf{p}_2 - \mathbf{p}_r\| \tag{3}$$

For forward kinematics, the position must satisfy:

$$\|\mathbf{p}_r - \mathbf{p}_1\|^2 = l_1^2 \tag{4}$$
$$\|\mathbf{p}_r - \mathbf{p}_2\|^2 = l_2^2 \tag{5}$$

Since two equations cannot fully determine the 6-DOF state, gravity and wheel-leg ground contact act as additional constraints to yield a unique solution.

The velocity kinematics relate the robot body motion to the ascender port velocities. Applying rigid-body kinematics to the left and right ports:

$$\mathbf{v}_{\text{ascL}} = \mathbf{v}_{\text{body}} - \mathbf{r}_{\text{L,asc}} \times \boldsymbol{\omega}_{\text{body}} \tag{6}$$
$$\mathbf{v}_{\text{ascR}} = \mathbf{v}_{\text{body}} - \mathbf{r}_{\text{R,asc}} \times \boldsymbol{\omega}_{\text{body}} \tag{7}$$

where $\mathbf{v}_{\text{ascL}}$, $\mathbf{v}_{\text{ascR}}$ are the left and right port velocities [m/s], and $\mathbf{r}_{\text{L,asc}}$, $\mathbf{r}_{\text{R,asc}}$ are the position vectors from the robot center to each port [m]. In matrix form:

$$\begin{bmatrix}\mathbf{v}_{\text{ascL}}\\ \mathbf{v}_{\text{ascR}}\end{bmatrix} = \underbrace{\begin{bmatrix}\mathbf{I} & -[\mathbf{r}_{\text{L,asc}}]_\times\\ \mathbf{I} & -[\mathbf{r}_{\text{R,asc}}]_\times\end{bmatrix}}_{\mathbf{J}_{\text{asc}}} \begin{bmatrix}\mathbf{v}_{\text{body}}\\ \boldsymbol{\omega}_{\text{body}}\end{bmatrix} \tag{8}$$

where $[\mathbf{r}]_\times$ denotes the skew-symmetric matrix of vector $\mathbf{r}$. The inverse relationship is obtained via pseudo-inverse:

$$\begin{bmatrix}\mathbf{v}_{\text{body}}\\ \boldsymbol{\omega}_{\text{body}}\end{bmatrix} = \mathbf{J}_{\text{asc}}^{\dagger} \begin{bmatrix}\mathbf{v}_{\text{ascL}}\\ \mathbf{v}_{\text{ascR}}\end{bmatrix} \tag{9}$$

where $\mathbf{J}_{\text{asc}}^{\dagger} = (\mathbf{J}_{\text{asc}}^T\mathbf{J}_{\text{asc}})^{-1}\mathbf{J}_{\text{asc}}^T$.

To quantitatively evaluate workspace performance, four indices are defined via SVD of $\mathbf{J}_{\text{asc}} = \mathbf{U}\boldsymbol{\Sigma}\mathbf{V}^T$:

$$\kappa(\mathbf{p}_r) = \frac{\sigma_{\max}}{\sigma_{\min}} \quad \text{(Condition Number)} \tag{10}$$

$$\mu_{\text{norm}}(\mathbf{p}_r) = \frac{\prod_i \sigma_i}{\max \prod_i \sigma_i} \quad \text{(Manipulability)} \tag{11}$$

where $L_1 = \|\mathbf{p}_r - \mathbf{p}_1\|$, $L_2 = \|\mathbf{p}_r - \mathbf{p}_2\|$, and $L_{\max}$ is the maximum allowable rope length [m].

As shown in Fig. 4, all indices show optimal values in the central workspace region and degrade toward the boundaries. Critically, $\sigma_{\min} > 0$ throughout the entire workspace, confirming that no mathematical singularities exist within the suspension zone. This IRPM characteristic eliminates the need for complex singularity avoidance algorithms required in fully constrained cable robots.

B. WHEEL-LEG ANALYSIS

The wheel-leg system serves three key functions on the integrated platform: high-speed movement via wheels within the ascender-defined workspace; perpendicular position determination through COM stability analysis within the support polygon formed by the wheel contact points; and rollover prevention and exterior wall damage minimization

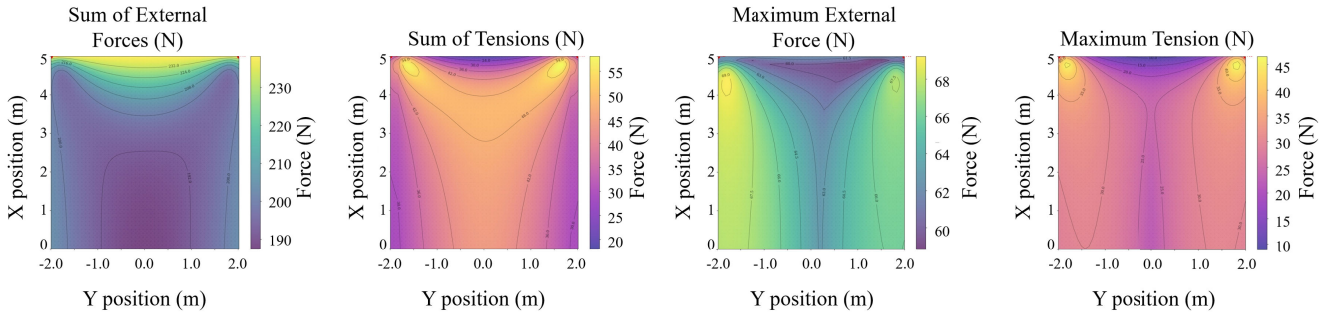

FIGURE 5. Distribution analysis of ground reaction force (GRF) and rope tension across the workspace. Ground reaction force varies between 190-240 N with minimum values in the central lower region, while rope tension ranges 20-55 N with maximum values in the upper central area.

through ground reaction force and rope tension distribution analysis.

The wheel-leg robot consists of a body with 6-DOF, four legs each with three rotational joints (Hip-Z, Hip-Y, Knee), and four wheels, giving a total of 22 joint DOF. The generalized coordinates are defined as:

$$\mathbf{q}_{\text{all}} = [\mathbf{q}_{\text{base}}, \mathbf{q}_{\text{leg}}, \mathbf{q}_{\text{wheels}}]^T \tag{12}$$

where $\mathbf{q}_{\text{base}} \in \mathbb{R}^6$, $\mathbf{q}_{\text{leg}} \in \mathbb{R}^{12}$, and $\mathbf{q}_{\text{wheels}} \in \mathbb{R}^4$. Kinematic analysis employs four coordinate frames: global $\{G\}$, body $\{B\}$, leg $\{L_i\}$, and wheel $\{W_i\}$, with inter-frame transformations defined via DH parameters. The wheel motion is governed by the nonslip pure rolling constraint, requiring zero relative velocity at each contact point:

$$\mathbf{v}_{\text{contact},i} = \mathbf{v}_{\text{wheel_center},i} - r_w \dot{\theta}_{w,i} \mathbf{t}_i = \mathbf{0} \tag{13}$$

where r_w is the wheel radius [m], $\dot{\theta}_{w,i}$ is the wheel angular velocity [rad/s], and $\mathbf{t}_i$ is the unit rolling direction vector at the i-th contact point.

Forward kinematics computes the wheel position and orientation from the joint angles via chain transformation:

$$\boldsymbol{\xi}_{\text{wheel}} = \mathbf{H}_{\text{wheel}} \mathbf{H}_{\text{knee}} \mathbf{H}_{\text{hip-y}} \mathbf{H}_{\text{hip-z}} \mathbf{r}_{\text{COM}} \tag{14}$$

where $\mathbf{H}_{(\cdot)}$ are 4×4 homogeneous transformation matrices for each joint and $\mathbf{r}_{\text{COM}}$ is the COM position vector in the body frame [m]. The corresponding velocity relationship is:

$$\mathbf{v}_{\text{wheel}} = \mathbf{J}_{\text{wheel}} \dot{\mathbf{q}}_{\text{joint}} \tag{15}$$

and the inverse kinematics is obtained via pseudo-inverse:

$$\dot{\mathbf{q}}_{\text{joint}} = \mathbf{J}^{\dagger}_{\text{wheel}} \mathbf{v}_{\text{wheel}} \tag{16}$$

The contact point velocity of the i-th wheel is related to the body motion by rigid-body kinematics:

$$\mathbf{v}_{\text{contact},i} = \mathbf{v}_{\text{body}} - [\mathbf{r}_i]_\times \boldsymbol{\omega}_{\text{body}} \tag{17}$$

Assembling all four contact points into matrix form:

$$\mathbf{v}_{\text{contact}} = \underbrace{\begin{bmatrix} \mathbf{I}_3 & -[\mathbf{r}_1]_\times \\ \mathbf{I}_3 & -[\mathbf{r}_2]_\times \\ \mathbf{I}_3 & -[\mathbf{r}_3]_\times \\ \mathbf{I}_3 & -[\mathbf{r}_4]_\times \end{bmatrix}}_{\mathbf{A}_{\text{contact}}} \boldsymbol{\xi}_{\text{body}} \tag{18}$$

where $\mathbf{A}_{\text{contact}}$ is a 12×6 contact velocity mapping matrix, and the inverse relationship is $\boldsymbol{\xi}_{\text{body}} = \mathbf{A}^{\dagger}_{\text{contact}} \mathbf{v}_{\text{contact}}$.

The inverse relationship is $\boldsymbol{\xi}_{\text{body}} = \mathbf{A}^{\dagger}_{\text{contact}} \mathbf{v}_{\text{contact}}$. The body position is then updated via Euler integration:

$$\mathbf{r}_{\text{body},n+1} = \mathbf{r}_{\text{body},n} + \boldsymbol{\xi}_{\text{body}} \cdot dt \tag{19}$$

where dt denotes the time interval [s].

To evaluate static stability, the Normalized Energy Stability Margin (NESM) is defined as:

$$\text{NESM} = \frac{d_{\min}}{d_{\max}} \tag{20}$$

where $d_{\min}$ is the shortest distance from the COM to the support polygon boundary [m] and $d_{\max}$ is the maximum distance within the support polygon [m]. On a slope with inclination angle α, the support polygon is projected in the direction of gravity for calculation. A comprehensive stability analysis incorporating rope tension effects will be addressed in future work.

In a hybrid robot system, the ground reaction forces and cable tensions must satisfy static equilibrium conditions. The force and moment equilibria of the entire system are expressed as follows:

Force Equilibrium:

$$\sum_{i=1}^{n_{\text{cables}}} T_i \frac{\mathbf{l}_i}{|\mathbf{l}_i|} + \sum_{j=1}^{n_{\text{contacts}}} \mathbf{F}_{\text{GRF},j} + m\mathbf{g} = \mathbf{0} \tag{21}$$

Moment Equilibrium:

$$\sum_{i=1}^{n_{\text{cables}}} T_i (\mathbf{r}_{c,i} \times \frac{\mathbf{l}_i}{|\mathbf{l}_i|}) + \sum_{j=1}^{n_{\text{contacts}}} (\mathbf{r}_{g,j} \times \mathbf{F}_{\text{GRF},j}) = \mathbf{0} \tag{22}$$

where T_i is the i-th cable tension [N], $\mathbf{l}_i$ is the i-th cable direction vector [m], $|\mathbf{l}_i|$ is the cable length [m], $\mathbf{F}_{\text{GRF},j}$ is the ground reaction force vector at the j-th contact point [N], $\mathbf{r}_{c,i}$ is the position vector from the body center to the i-th cable attachment point [m], $\mathbf{r}_{g,j}$ is the position vector from the body center to the j-th ground contact point [m], m is the total robot mass [kg], $\mathbf{g}$ is the gravitational acceleration vector [m/s^2], n_{cables} is the number of cables, and n_{contacts} is the number of contact points.

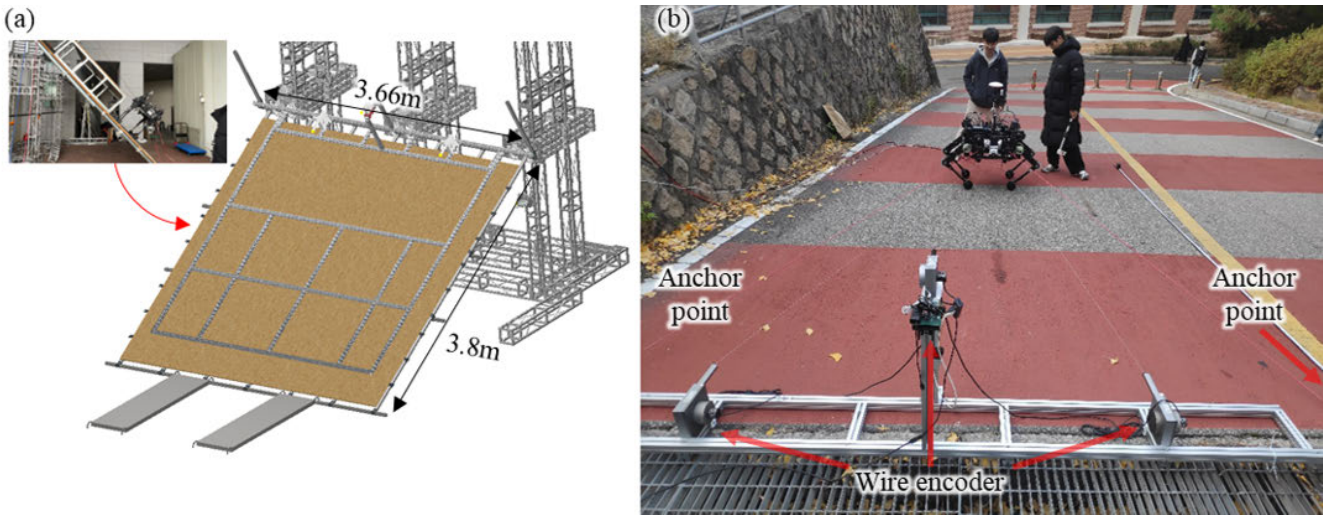

FIGURE 6. Experimental environments used in the demonstration. (a) Test bench (b) Outdoor experimental site for water cleaning and GPS reception. Wire encoder and anchor point positions for position measurement.

The structure matrix $\mathbf{A}_{\text{Tension}}$ is defined as follows:

$$\mathbf{A}_{\text{Tension}} = \begin{bmatrix} \frac{\mathbf{l}_1}{|\mathbf{l}_1|} & \frac{\mathbf{l}_2}{|\mathbf{l}_2|} & \cdots \\ \mathbf{r}_{c,1} \times \frac{\mathbf{l}_1}{|\mathbf{l}_1|} & \mathbf{r}_{c,2} \times \frac{\mathbf{l}_2}{|\mathbf{l}_2|} & \cdots \end{bmatrix} \tag{23}$$

where $\mathbf{A}_{\text{Tension}}$ is a $6\times n_{\text{cables}}$ tension-structure matrix.

The tension distribution problem is expressed as follows:

$$\mathbf{A}_{\text{Tension}}\mathbf{T} = -\mathbf{f}_{\text{ext}} \tag{24}$$

where $\mathbf{T} = [T_1, T_2, \ldots, T_{n_{\text{cables}}}]^T$ is an $n_{\text{cables}}\times 1$ cable tension vector [N], and $\mathbf{f}_{\text{ext}}$ is a 6×1 external force vector including gravity and ground reaction forces [N, Nm].

When this system is overconstrained, the least-squares solution is

$$\mathbf{T}_{\text{min}} = \mathbf{A}^{\dagger}_{\text{Tension}}\mathbf{f}_{\text{ext}} \tag{25}$$

where $\mathbf{A}^{\dagger}_{\text{Tension}}$ is an $n_{\text{cables}}\times 6$ pseudo-inverse function.

According to the analysis results shown in Figure 5, the ground reaction force (GRF) varies between 190 N and 240 N, with the lowest value of approximately 190 N shown in the central lower region of the slope. The rope tension distribution varies in the range of 20–55 N, with maximum values observed in the upper-central part of the slope. By synthesizing these data, the central lower section of the slope was determined to be the most efficient section for robot operation.

IV. PERFORMANCE EVALUATION AND EXPERIMENTAL RESULTS

Individual component and integrated system tests were conducted sequentially in controlled laboratory environments and outdoor testbeds, in collaboration with the Korea Institute of Machinery & Materials (KIMM). The test environment consisted of a test bench and an outdoor experimental environment, as shown in Figure 6. This staged procedure reduces the overall verification effort by identifying subsystem-level issues before conducting full-system integration tests.

A. ASCENDING AND DESCENDING VELOCITY TEST

Vertical movement speed was evaluated by raising and lowering the robot on a 3 m test bench, with position data collected at 10 ms intervals using a wire encoder (KS90D, precision: 0.03 mm/pulse). The ascending and descending speeds averaged 21.84 m/min and 22.93 m/min, respectively, with the approximately 5% higher descent speed attributed to gravitational assistance. Steady-state speed deviation remained within ±2% after an initial 2 s acceleration phase. The result is as illustrated in the Figure 8.

B. OBSTACLE OVERCOMING PERFORMANCE

Climbing capability was evaluated using 500 mm standard obstacles at various approach angles. All trials were successful, with a maximum COM height change of 195 mm. Stable climbing was achieved through sequential leg actuation in a gallop-type locomotion pattern, as illustrated in Figure 7.

C. POSITION ESTIMATION ACCURACY

Position estimation accuracy was evaluated by comparing multisensor fusion (wire encoder, GPS, IMU) against a Total Station reference, with coordinate alignment via Horn's method and Kabsch algorithm optimization. Average accuracy was 7.30 cm, with RMSE within ±5 cm per axis. Primary error sources were rope elastic deformation and GPS multipath effects, with improvement expected through future vision-based SLAM integration. The results are illustrated in Figure 9.

D. WORKING MODULE PERFORMANCE

To evaluate the actual work performance of the robot, the work speed was measured by mounting cleaning modules.



FIGURE 7. Demonstration on overcoming a 500 mm obstacle using a test bench. (a) Initial position. (b) Left front leg elevation. (c) Right front leg elevation. (d) Forward movement before body elevation. (e) Body elevation over obstacle. (f) Rear left leg elevation. (g) Rear right leg elevation. (h) Complete forward movement.

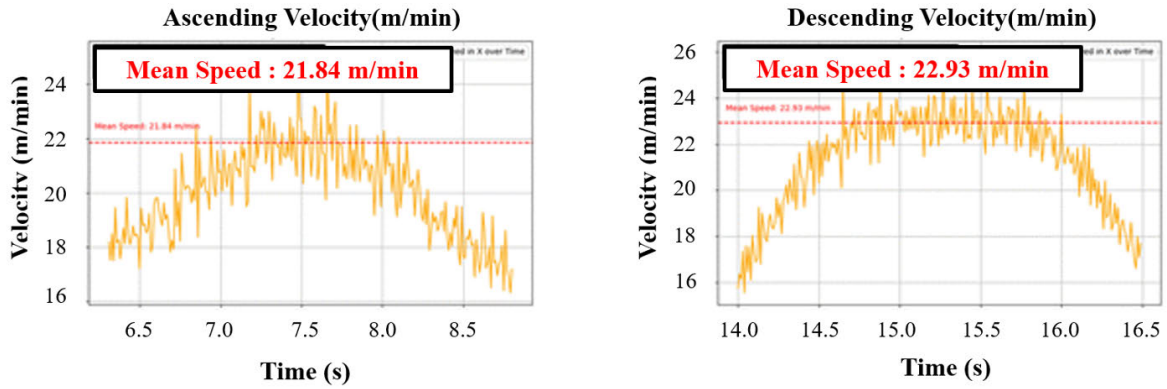

FIGURE 8. Maximum velocity measurement results during ascending and descending.

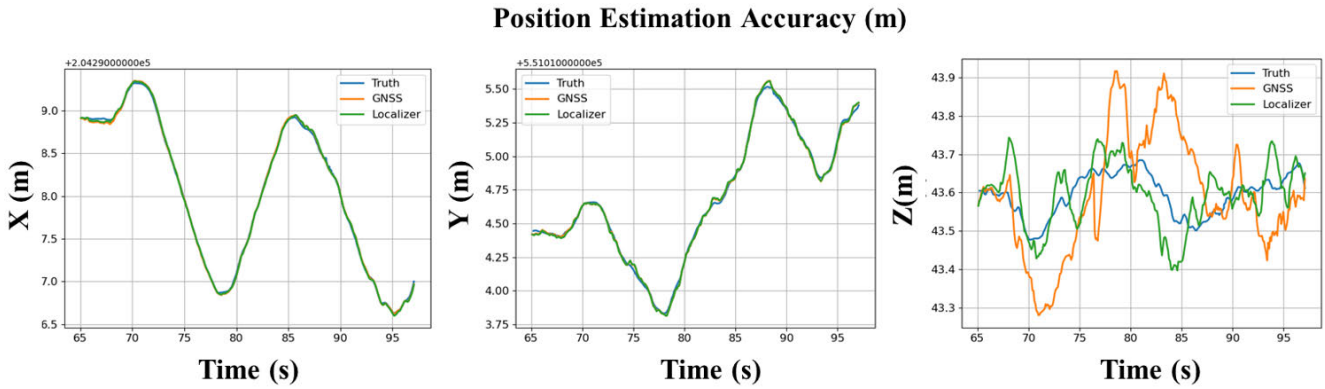

FIGURE 9. Position estimation accuracy comparison across X, Y, and Z axes. Truth (blue), GNSS (orange), and Localizer (green) trajectories are compared over time.

Cleaning work was performed on a simulated exterior wall of 0.6 m × 7.94 m in size, calculating the processed area per unit time. Experiments were conducted considering appropriate movement speeds to maintain the work quality.

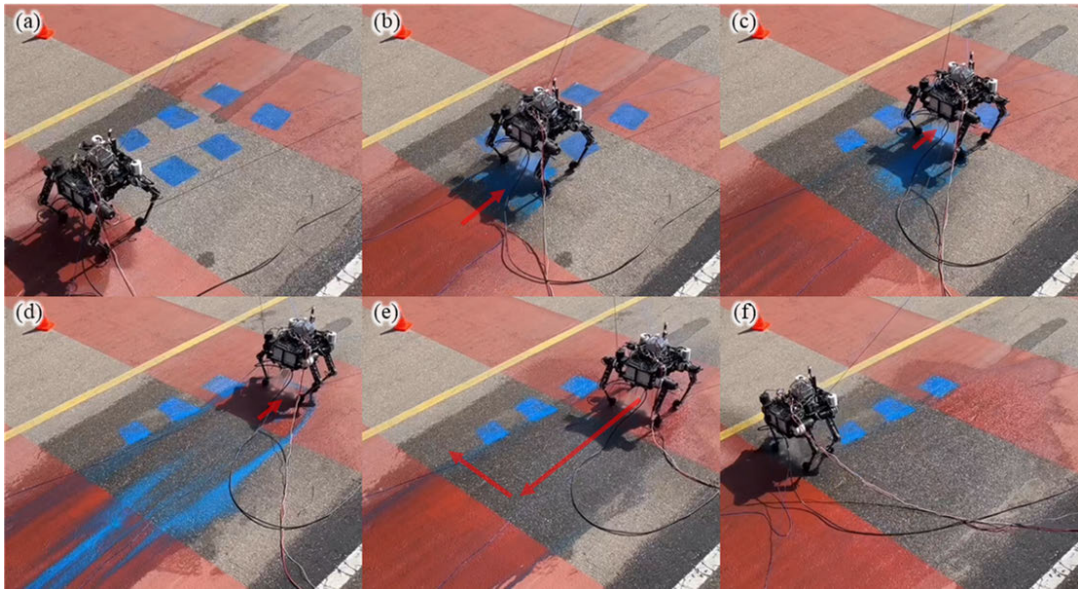

FIGURE 10. Cleaning work test in outdoor environment. (a) Cleaning starts. (b) First contaminant washing. (c) Second contaminant washing. (d) Third contaminant washing. (e) Position movement after cleaning. (f) Cleaning completion. Comparison with contaminants.

Experimental results showed that the maximum working speed was measured at 4.8 m^2/min. In practice, it is common for speeds lower than the theoretical maximum speed to be applied because of factors such as obstacle avoidance and direction changes. The cleaning process is shown in Figure 10.

V. CONCLUSION

In this study, a hybrid robot platform integrating an ascender system and wheel-leg system was developed to address insufficient wall surface adaptation capability and workspace limitations of existing ascender robots.

Through IRPM characteristic analysis, no mathematical singularities were confirmed within the ascender workspace, and system performance was quantitatively evaluated using condition number and manipulability. For the wheel-leg system, kinematic analysis of the insect-type structure was performed to derive obstacle overcoming capability and rollover prevention conditions.

Performance tests of the 79.75 kg platform achieved vertical movement speed of 21.84 m/min, position control error of 7.3cm, maximum obstacle overcoming height of 500 mm, and maximum working speed of 4.8 m^2/min, satisfying the basic requirements for building exterior wall-cleaning tasks. Wind resistance was confirmed stable up to 9.4 m/s, with stronger wind performance expected based on current results.

However, the system has limitations: GPS-based position estimation may degrade in high-rise or complex environments, and the 79.75 kg system weight requires improvement in portability and installation convenience. In addition, working speeds lower than the measured theoretical performance are expected under actual field conditions due to safety and work quality considerations.

Future work includes vision-based SLAM integration for improved position estimation, lightweight redesign, and trajectory optimization for efficient path planning in complex façade environments. Long-term demonstration tests in actual high-rise buildings are required to verify reliability, with the aim of developing the system into a practical building maintenance automation solution.

ACKNOWLEDGMENT

(Sahoon Ahn and Yecheol Moon contributed equally to this work.)

REFERENCES

[1] O. Mitchell. (May 2018). *Skyscraper Window Washing Ripe for Automation*. [Online]. Available: https://www.therobotreport.com/high-rise-window-cleaning-ripe-automation/

[2] J. Lindner. (Jul. 2024). *Exploring Key Window Cleaning Industry Statistics for Market Trends*. [Online]. Available: https://gitnux.org/window-cleaning-industry-statistics/

[3] Parliament of the United Kingdom. (1972). *Defective Premises Act 1972*. [Online]. Available: https://www.legislation.gov.uk/ukpga/1972/35.

[4] E. Dotter. (Jan. 2021). *Window Washers*. [Online]. Available: https://www.healthday.com/a-to-z-health/public-health/window-washers-646930.html

[5] South China Morning Post. (2022). *2 Workers in Gondola Plunge More Than 20 Floors to Their Deaths in Hong Kong*. [Online]. Available: https://www.scmp.com/news/hong-kong/society/article/3181483/2-workers-gondola-plunge-more-20-floors-their-deaths-hong

[6] Stomp. (2023). *SCDF Rescues Two Workers Stranded on Gondola at 40th Floor of Capital Tower*. [Online]. Available: https://www.stomp.sg/singapore-seen/scdf-rescues-two-workers-stranded-on-gondola-at-40th-floor-of-capital-tower-in

[7] I. Y. Choi. (2024). *Worker Dies in Fall at Lotte Hotel World Remodeling Site*. [Online]. Available: https://news.kbs.co.kr/news/pc/view/view.do?ncd=8119268

[8] T. Seo, Y. Jeon, C. Park, and J. Kim, "Survey on glass and Façade-cleaning robots: Climbing mechanisms, cleaning methods, and applications," *Int. J. Precis. Eng. Manuf.-Green Technol.*, vol. 6, no. 2, pp. 367–376, Apr. 2019.
[9] H. Zhang, J. Zhang, and G. Zong, "Effective nonlinear control algorithms for a series of pneumatic climbing robots," in *Proc. IEEE Int. Conf. Robot. Biomimetics*, Jun. 2006, pp. 994–999.
[10] T. Miyake, H. Ishihara, and T. Tomino, "Vacuum-based wet adhesion system for wall climbing robots -lubricating action and seal action by the liquid-," in *Proc. IEEE Int. Conf. Robot. Biomimetics*, Feb. 2009, pp. 1824–1829.
[11] H. Zhang, W. Wang, R. Liu, J. Zhang, and G. Zong, "Locomotion realization of an autonomous climbing robot for elliptic half-shell cleaning," in *Proc. 2nd IEEE Conf. Ind. Electron. Appl.*, May 2007, pp. 1220–1225.
[12] T. Seo and M. Sitti, "Tank-like module-based climbing robot using passive compliant joints," *IEEE/ASME Trans. Mechatronics*, vol. 18, no. 1, pp. 397–408, Feb. 2013.
[13] S. Yoo, T. Kim, M. Seo, J. Oh, J. Kim, H. S. Kim, and T. Seo, "Modeling and verification of multi-winding rope winch for facade operation," *Mechanism Mach. Theory*, vol. 155, Jan. 2021, Art. no. 104105.
[14] S. Yoo, I. Joo, J. Hong, J. Kim, H. S. Kim, and T. Seo, "Mechanical and empirical parameter design on a multi-wound differential pulley winch for a wall-climbing robot," *Int. J. Precis. Eng. Manuf.*, vol. 21, no. 5, pp. 857–867, May 2020.
[15] M. Seo, S. Yoo, M. Choi, J. Oh, H. S. Kim, and T. Seo, "Vibration reduction of flexible rope-driven mobile robot for safe Façade operation," *IEEE/ASME Trans. Mechatronics*, vol. 26, no. 4, pp. 1812–1819, Aug. 2021.
[16] M. Choi, S. Ahn, H. S. Kim, and T. Seo, "Modeling and control of TRDMR on a facade with thruster-driven adhesion," *Mechatronics*, vol. 94, Oct. 2023, Art. no. 103038.
[17] K. Lee, K. Ko, S. Park, H. S. Kim, and T. Seo, "Obstacle-overcoming and stabilization mechanism of a rope-riding mobile robot on a Façade," *IEEE Robot. Autom. Lett.*, vol. 7, no. 2, pp. 1372–1378, Apr. 2022.
[18] H. Chae, Y. Moon, K. Lee, S. Park, H. S. Kim, and T. Seo, "A tethered Façade cleaning robot based on a dual rope windlass climbing mechanism: Design and experiments," *IEEE/ASME Trans. Mechatronics*, vol. 27, no. 4, pp. 1982–1989, Aug. 2022.
[19] J. Lee, H. Chae, K. Kim, H. S. Kim, and T. Seo, "Detection method for transparent window cleaning device, image processing approach," *Sci. Rep.*, vol. 12, no. 1, p. 3229, Feb. 2022.
[20] *Spotmini, Boston Dynamics, Robot*. Waltham, MA, USA: B. Dynamics, Wikimedia Commons, 2019.
[21] *Anymal—AI-based Robot Dog*. Zürich, Switzerland: ANYbotics, 2022.
[22] S. Kitano, S. Hirose, A. Horigome, and G. Endo, "Titan-XIII: Sprawling-type quadruped robot," *Robomech J.*, vol. 3, pp. 1–16, Mar. 2016.
[23] J. Hooks, M. S. Ahn, J. Yu, X. Zhang, T. Zhu, and H. Chae, "Alphred: A multimodal operations quadruped robot," *IEEE Robot. Autom. Lett.*, vol. 5, no. 4, pp. 5409–5416, Apr. 2020.
[24] K. Lee, S. Ahn, J. Yang, H. Kim, and T. Seo, "Rope on rope: Reducing residual vibrations in rope-based anchoring system and rope-driven Façade operation robot," *Sensors*, vol. 25, no. 8, p. 2463, Apr. 2025.



SAHOON AHN received the B.S. degree in mechanical engineering from Hanyang University, South Korea, in 2021, where he is currently pursuing the Ph.D. degree in mechanical engineering. His research interest includes quadruped robot control.



YECHEOL MOON received the B.S. degree in mechanical engineering and the M.S. and Ph.D. degrees in convergence mechanical engineering from Hanyang University, South Korea, in 2018, 2020, and 2025, respectively. He is currently a Senior Researcher with the Advanced Robotics Research Center, Korea Institute of Machinery and Materials (KIMM), Daejeon, South Korea. His research interests include robot systems architecture, multibody dynamics, whole-body control, legged and humanoid robots, and robot teleoperation.



JOONHYUK KWON received the B.S. degree in mechanical engineering from Hanyang University, South Korea, in 2022, where he is currently pursuing the Ph.D. degree in mechanical engineering. His research interests include the design and control of robotic mechanisms.



JIHONG KIM received the B.S. degree in electronic engineering from Kyonggi University, South Korea, in 2024. He is currently pursuing the Ph.D. degree in mechanical engineering with Hanyang University. His research interest includes robot control.



HYUNGCHAN JOO received the B.S. degree in mechanical engineering from Hanyang University, South Korea, in 2024, where he is currently pursuing the M.S. degree in mechanical engineering. His research interests include robotic control and stability.



DOYOUNG PARK received the B.S. degree in mechanical engineering from Hanyang University, South Korea, in 2025, where he is currently pursuing the integrated M.S.–Ph.D. degree in mechanical convergence engineering. His research interest includes quadruped robot control.



HWA SOO KIM (Senior Member, IEEE) received the B.S. and Ph.D. degrees in mechanical engineering from Seoul National University, South Korea, in 2000 and 2006, respectively. He is currently an Associate Professor with the Department of Mechanical System Engineering, Kyonggi University, South Korea. His research interests include the design, modeling, and control of various mobile platforms for wall cleaning and stair climbing.



TAEWON SEO (Senior Member, IEEE) received the B.S. and Ph.D. degrees from the School of Mechanical and Aerospace Engineering, Seoul National University, South Korea, in 2003 and 2008, respectively. He is currently an Associate Professor with the School of Mechanical Engineering, Hanyang University, South Korea. Before joining Hanyang University, he was a Postdoctoral Researcher with the Nanorobotics Laboratory, Carnegie Mellon University; a Visiting Professor with the Biomimetic Millisystems Laboratory, University of California, Berkeley; a Visiting Scholar with the University of Michigan; and an Associate Professor with Yeungnam University, South Korea. His research interests include robot design, analysis, control, optimization, and planning. He received the Best Paper Award from the IEEE/ASME Transactions on Mechatronics, in 2014. He is a Technical/Associate Editor of IEEE/ASME Transactions on Mechatronics and *Intelligent Service Robots* and an Associate Editor of IEEE Robotics and Automation Letters.